Applied Thermal Engineering 91 (2015) 318–333

Contents lists available at ScienceDirect

Applied Thermal Engineering

journal homepage: www.elsevier.com/locate/apthermeng

Research paper

Role of cross-drilled holes in enhanced cooling of ventilated brake discs

H.B. Yan [a, b], S.S. Feng [b, c], X.H. Yang [b, d], T.J. Lu [b, c, *]

[a] School of Energy and Power Engineering, Xi'an Jiaotong University, Xi'an 710049, PR China
[b] MOE Key Laboratory for Multifunctional Materials and Structures, Xi'an Jiaotong University, Xi'an 710049, PR China
[c] State Key Laboratory for Strength and Vibration of Mechanical Structures, Xi'an Jiaotong University, Xi'an 710049, PR China
[d] Department of Building Environment and Energy Engineering, Xi'an Jiaotong University, Xi'an 710049, PR China

HIGHLIGHTS

- A thorough comparison between standard and cross-drilled brake discs is presented.
- Modification of internal and external flows by cross-drilled holes is clarified.
- Modification of local heat transfer pattern by cross-drilled holes is clarified.
- Substantially improved brake disc cooling can be achieved by cross-drilled holes.
- Mechanisms for cooling performance improvement by cross-drilled holes are quantified.

ARTICLE INFO

Article history:
Received 7 April 2015
Accepted 1 August 2015
Available online 28 August 2015

Keywords:
Ventilated brake disc
Radial vane
Cross-drilled hole
Rotating flow
Heat transfer enhancement

ABSTRACT

As constructive guidance for brake design engineers to improve brake disc cooling, understanding of thermo-fluidic behaviors associated with ventilated brake discs has attracted much attention. In this study, a systematic comparison of the thermo-fluidic characteristics between standard and cross-drilled ventilated brake discs incorporating radial vanes is carried out using numerical simulations. Mechanisms for heat transfer enhancement by the cross-drilled holes are clarified. To validate the numerical model, a series of experiments are also conducted. The gradient of axial pressure is found to drive the cooling air into the ventilated channel through cross-drilled holes. Such a special flow accelerates external boundary layer flow over the rubbing surface, enhancing therefore local heat transfer. Additionally, the through-hole flow removes heat via the surfaces of the holes while air jets issuing from the cross-drilled holes deflect to suction sides of the vanes, improving further local heat transfer. However, blockage by the jets not only reduces the pumping capacity through ventilated channel inlet but also causes a low-momentum wake downstream each jet. Hence, local heat transfer on the inner surface of each rubbing disc is deteriorated. Eventually, relative to the standard brake disc, the cross-drilled brake disc exhibits a 22–27% higher overall Nusselt number within the typical operating range of 200–1000 RPM. The contribution of each mechanism to overall heat transfer enhancement is quantified.

© 2015 Elsevier Ltd. All rights reserved.

1. Introduction

Contemporary passenger vehicles employ prevalently disc brakes as illustrated in Fig. 1(a). During braking, the kinetic and potential energy of the vehicle is transformed into thermal energy by sliding friction between the brake disc and the pads. To prevent vaporization of the brake fluid [1], heat conduction to the brake pads is purposely minimized. Therefore, approximately 90% of frictional heat is transferred to the brake discs [2]. As reported by Palmer et al. [3] and Pevec et al. [4], high-load braking can raise the disc temperature up to 600 °C. Numerous studies have revealed that such overheating can result in or aggravate brake fade [5–7], increased wear of friction pair [8], brake disc coning and thermal fatigue cracking [9–11], as well as thermal judder of the brake system [12]. Therefore, sufficient cooling of the brake disc is crucial to ensure brake reliability and comfort, especially for higher performance passenger vehicles.

* Corresponding author. MOE Key Laboratory for Multifunctional Materials and Structures, Xi'an Jiaotong University, Xi'an 710049, PR China.
E-mail address: tjlu@mail.xjtu.edu.cn (T.J. Lu).

http://dx.doi.org/10.1016/j.applthermaleng.2015.08.042
1359-4311/© 2015 Elsevier Ltd. All rights reserved.

Nomenclature

A	surface area (m^2)
A_{ref}	reference surface area (m^2)
C_1, C_2	coefficients defined in Eq. (11)
d_h	diameter of circular cross-drilled holes (m)
h	local heat transfer coefficient defined in Eq. (4) (W/(m^2K))
h_e	local effective heat transfer coefficient defined in Eq. (3) (W/(m^2K))
H_{hb1}, H_{hb2}	axial dimensions of a brake hub (m)
H_v	height of vanes (m)
k	thermal conductivity of air (W/(mK))
L_{v1}, L_{v2}	lengths of long and short vanes (m)
m	mass flow rate of cooling air (kg/s)
N	rotational speed of a brake disc (RPM)
Nu	local Nusselt number defined in Eq. (5)
Nu_e	local effective Nusselt number defined in Eq. (2)
$Nu_{overall}$	overall Nusselt number defined in Eq. (6)
p	pressure (Pa)
P_h, P_v	perimeters of hole cross-section and vane cross-section, respectively (m)
q"	local heat flux (W/m^2)
Q	heat transfer rate (W)
Q_t	total power input (W)
r	radial coordinate (m)
Re	rotational Reynolds number defined in Eq. (1)
R_{h1}–R_{h3}	radial locations of cross-drilled holes (m)
R_{hb1}, R_{hb2}	radial dimensions of a brake hub (m)
R_{ri}, R_{ro}	inner and outer radii of inboard disc (m)
R_v	radial location of vanes (m)
s	local curvilinear coordinate (m)
t	time (s)
t_r	thickness of a rubbing disc (m)
t_v	thickness of vanes (m)
T	wall temperature (°C)
T_a	ambient air temperature (°C)
V	magnitude of relative velocity (m/s)
y^+	dimensionless wall distance
z	axial coordinate (m)

Greek symbols

ε	emissivity of a matt black paint
η	contribution of separate mechanism to overall heat transfer enhancement defined in Eq. (13)
θ	azimuth coordinate (rad)
θ_0	geometric periodic angle of a brake disc (rad)
μ	dynamic viscosity of air (Pa·s)
ρ	density of air (kg/m^3)
σ	Stefan–Boltzmann constant ($W/(m^2K^4)$)
ω	angular velocity magnitude of a brake disc (rad/s)

Subscripts (lowercase) and abbreviations (capital)

hs, HS	hole surface of inboard disc
irs, IRS	inner rim surface of inboard disc
is, IS	inner surface of inboard disc
m	area-averaged value
ors, ORS	outer rim surface of inboard disc
rs, RS	rubbing surface of inboard disc
RPM	revolutions per minute
vs, VS	vane surface

To effectively remove frictional heat, centrifugal fan-like ventilated brake discs as illustrated in Fig. 1 have been devised. Relative to a solid brake disc, substantially improved cooling can be achieved by internal forced convection through the ventilated channel [13]. Regardless of the cross-section and configuration of heat dissipation elements sandwiched between the rubbing discs, commercially available ventilated brake discs may be classified into standard and cross-drilled brake discs as shown in Fig. 1(b) and (c), respectively [14].

Ever since the popular application of brake discs in the 1960s [15], considerable theoretical and experimental efforts have been devoted to understanding the thermo-fluidic characteristics and improving the cooling performance of standard brake discs as reviewed in Ref. [16]. In comparison, however, thermo-fluidic insight about high performance cross-drilled brake discs is limited in the open literature. Focusing on the overall performance, Wallis [17] conducted dynamometer testing of standard and cross-drilled radial vane ventilated brake discs. It was found that cross-drilled holes shortened the stopping distance of a vehicle for a given brake pressure, and reduced brake disc temperature. On-vehicle test by Antanaitis et al. [18] revealed superior cooling performance of cross-drilled brake discs compared with standard ones. With respect to local fluid flow behaviors, Barigozzi et al. [19] measured the distribution of axial velocity component near the rubbing surface of a cross-drilled brake disc by laser Doppler anemometry. They reported that cooling air was drawn into the ventilated channel through these holes. However, the influence of cross-drilled holes on external (i.e., outside the ventilated channel) and internal (i.e., inside the ventilated channel) fluid flow and local heat transfer was not characterized in Ref. [19]; performance comparison with standard brake disc was also absent in Ref. [19]. It should also be mentioned that detailed geometric parameters of the investigated brake discs are not available in existing studies [17–19] due to confidentiality reasons. In view of the above, the thermo-fluidic mechanisms underlying the superior cooling performance of cross-drilled ventilated brake discs have not yet been fully understood. Such insights, however, act as constructive guidance for brake design engineers to further optimize the high performance cross-drilled brake discs.

This study, therefore, presents a comprehensive comparison of fluid flow and heat transfer characteristics between standard and cross-drilled radial vane brake discs having systematically controlled geometric parameters. Special focus is placed upon revealing: (a) how cooling air enters the ventilated channel through cross-drilled holes; (b) how this special flow modifies external and internal flows compared with a standard brake disc; (c) how the modified fluid flow affects local heat transfer pattern on brake disc surface; and (d) how the modified local heat transfer pattern quantitatively determines overall brake disc cooling performance. To this end, a series of steady-state and transient numerical simulations are performed for both standard and cross-drilled brake discs, with experiments conducted on standard brake disc to validate the numerical model.

2. Standard and cross-drilled ventilated brake discs

Fig. 2 illustrates schematically the standard and cross-drilled ventilated brake discs compared in the present study. They are

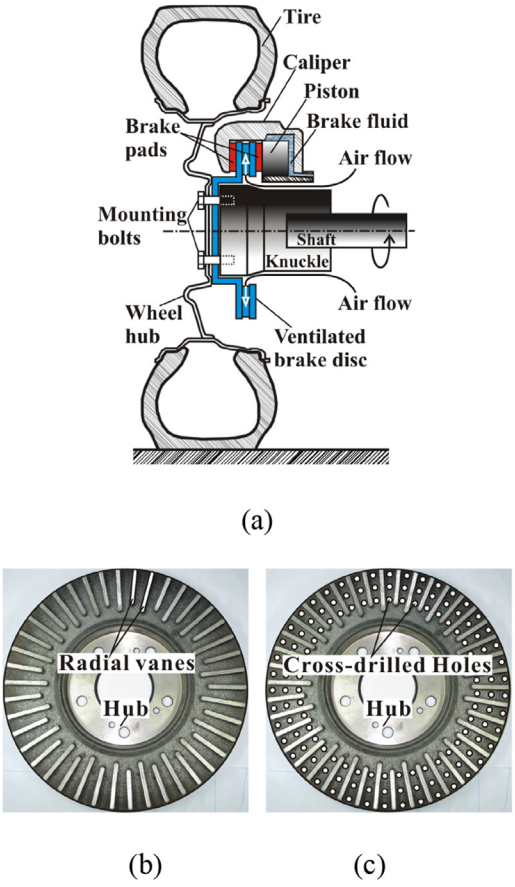

Fig. 1. Illustration of a passenger vehicle disc brake system: (a) working principle; (b) standard radial vane brake disc; (c) cross-drilled radial vane brake disc.

geometrically designed according to a commercially available radial vane brake disc prevalent for passenger vehicles, as shown in Fig. 1(b). Both brake discs have 42 alternatively arranged short and long radial vanes that protrude from the rubbing discs. These vanes have identical thickness (t_r) and have fillet at both the leading and trailing edges. In addition, the overall geometric dimensions of the rubbing discs and the hub are identical for both brake discs.

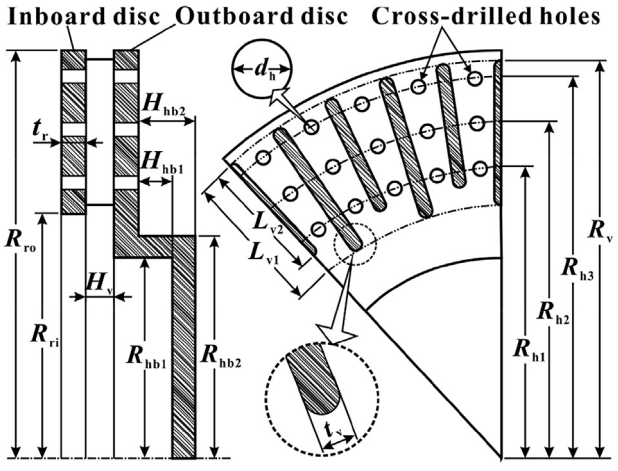

Fig. 2. Geometric details of the cross-drilled ventilated brake disc.

For the cross-drilled brake disc, in particular, three rows of circular holes with identical diameter (d_h) are drilled through both rubbing discs, as shown in Figs. 1(c) and 2. In total, 126 holes are drilled on each rubbing disc, with 42 holes in each row. These holes are arranged in an inline pattern along the radial direction. Azimuthally, each hole is located at the center of each cooling passage formed by two neighboring vanes. Detailed geometric parameters of the brake discs are depicted in Fig. 2 and summarized in Table 1.

In this comparative study via numerical simulations, both brake discs are assumed to be made of a prevalent grey cast iron (denoted as FC250 in Ref. [20]) for automobile brake discs. Density, specific heat and thermal conductivity of this material measured by Kim et al. [20] are 7220 kg/m^3, 503 J/(kgK) and 42 W/(mK), respectively.

3. Experimental details

To validate the present numerical model (see next section), a series of experiments are conducted on a standard brake disc. Although the test sample, facilities and test methods have been presented in a previous study [16], necessary experimental details relevant to the present numerical simulations are presented below for completeness.

3.1. Test sample and facilities

Given that the casting process endows the reference brake disc (see Fig. 1(b)) with large geometric uncertainties, the brake disc is duplicated using AISI 304 stainless steel according to the dimensions given in Table 1. To this end, the vanes are first fabricated by wire-electrode cutting and subsequently brazed onto the two rubbing discs in a vacuum furnace. Detailed brazing process and procedures are documented in Ref. [21]. The density, specific heat and thermal conductivity of stainless steel are 8000 kg/m^3, 500 J/(kgK) and 16.2 W/(mK) [22,23], respectively.

The purposely designed test rig for rotating heat transfer measurement is illustrated in Fig. 3. It contains a 3-phase AC motor and shafting mounted on a base frame. The motor is connected to a shaft through a flexible coupling. The shaft rotates on bearings and is flanged at the opposite end to allow mounting of the brake disc sample. Another dismountable shaft supported by two additional bearings is bolted to the former shaft on one end. This is used to allow a cylindrical Perspex component (modeling the knuckle, with a radius of $0.4R_{ro}$) and a four-channel slip ring to be mounted. As highlighted in Fig. 3, the knuckle is flush mounted with the outboard disc. The rotational speed of the brake disc is controlled by an inverter connected to the AC motor and measured with a digital tachometer.

3.2. Heat transfer measurement

To simulate frictional heating, two identical annular heating pads with identical inner and outer radii as those of the inboard rubbing disc are attached to both rubbing discs by a thermally

Table 1
Geometric parameters of the standard and cross-drilled radial vane brake discs depicted in Fig. 2.

Parameter	Value	Parameter	Value
d_h	5.0 mm	R_{h3}	140.0 mm
H_{hb1}	13.0 mm	R_{hb1}	74.0 mm
H_{hb2}	21.0 mm	R_{hb2}	82.0 mm
H_v	10.0 mm	R_{ri}	90.0 mm
L_{v1}	54.0 mm	R_{ro}	150.0 mm
L_{v2}	46.0 mm	R_v	147.0 mm
R_{h1}	108.0 mm	t_r	9.0 mm
R_{h2}	124.0 mm	t_v	5.0 mm

conductive double-sided tape. The tape has a thickness of ~0.1 mm and a thermal conductivity of ~1.5 W/(mK). Each heating pad, thickness 0.2 mm, is consisted of etched Inconel heating wires sandwiched by two Kapton films. Each Kapton film has a thickness of 0.076 mm and a thermal conductivity of 0.12 W/(mK) [24]. To remedy the non-uniformity of heat flux induced by the gaps between heating wires, copper foils with a thickness of 0.06 mm are attached to the heating pads. Consequently, a constant heat flux of 3640 W/m^2 is imposed, corresponding to a total power input of 329 W. A four channel slip ring connects these heating elements to an Agilent™ 6655A DC power supply.

An infrared camera (Fluke™ Ti50) is used to measure the temperature field on the inboard copper foil surface, which is sprayed with matte black paint to offer an emissivity of ~1.0. The resolution and frame rate of the infrared camera are 320 × 240 pixels and 60 Hz, respectively. Within radial span of the annular target surface (i.e., $R_{ro} - R_{ri}$), there are approximately 40 measurement points. Before testing, when the brake disc is stationary, the infrared camera is calibrated with a T-type foil thermocouple (Omega™) attached to the copper foil. For reference, an additional thermocouple is used to measure the ambient air temperature.

Two types of tests are conducted to evaluate transient and steady-state thermal behaviors of the brake disc, respectively. The transient test simulates continuous downhill braking at a constant vehicle speed. To this end, the brake disc is first accelerated to 800 RPM. Then the heating elements are switched on. Temperature field on the inboard copper foil surface is recorded every 60 s until steady-state heat transfer is approached. On the other hand, the steady-state tests aim to clarify the cooling performance of the brake disc at various rotational speeds from 200 RPM to 1000 RPM, corresponding to typical vehicle speeds of 25–124 km/h. For these tests, only the steady-state temperature field is measured. Detailed operating conditions of the experiments are summarized in Table 2.

3.3. Data reduction and measurement uncertainties

For transient results, temperature difference between the inboard copper foil surface and ambient air is used for interpretation. For steady-state results, the rotational Reynolds number (Re) and the effective Nusselt number (Nu_e) are used, defined as:

$$Re = \frac{\rho \omega R_{ro}^2}{\mu} \tag{1}$$

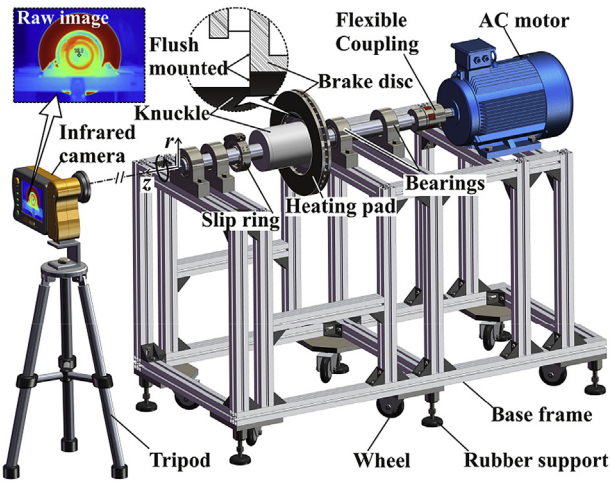

Fig. 3. Three-dimensional illustration of test facilities.

Table 2
Operating conditions of experiments.

Type of experiment	Transient	Steady-state
Rotational speed, N	800 RPM	200–1000 RPM
Ambient air temperature, T_a	10.3 °C	11.1–11.7 °C
Total power input, Q_t	329 W	329 W

$$Nu_e(r,\theta) = \frac{R_{ro} h_e(r,\theta)}{k} \tag{2}$$

where ρ, μ and k denote the density, dynamic viscosity and thermal conductivity of air, respectively; ω is the angular velocity magnitude of the rotating brake disc. h_e represents the effective heat transfer coefficient obtained on the inboard copper foil surface, defined as:

$$h_e(r,\theta) = \frac{Q_t \Big/ \left[2\pi\left(R_{ro}^2 - R_{ri}^2\right)\right]}{T_{rs}(r,\theta) - T_a} - \frac{\varepsilon\sigma\left[T_{rs}^4(r,\theta) - T_a^4\right]}{T_{rs}(r,\theta) - T_a} \tag{3}$$

where Q_t is the total power input by the heating elements; T_{rs} is the measured local wall temperature on the rubbing surface of the inboard disc; T_a is the ambient air temperature; ε is the emissivity of the matt black paint; and σ is Stefan–Boltzmann constant. For consistency with subsequent numerical simulations without considering thermal radiation, the radiation heat transfer coefficient is estimated [25] and subtracted as indicated by the second term on the right-hand side of Eq. (3).

An uncertainty analysis is performed using the root mean square method as detailed in Ref. [26]. The thermo-physical properties of air based on ambient pressure and temperature are used in data reduction, with their uncertainties neglected. The uncertainty of rotational speed is found to be less than 4 RPM, resulting in an uncertainty of less than 4.0% for the rotational Reynolds number (Re). Ambient air temperature (T_a) is measured by a T-type thermocouple (Omega™) with a resolution of 0.1 °C. For each test, the fluctuation of ambient temperature is measured to be less than 0.5 °C. The temperature measured by infrared camera shows a maximum deviation of 0.2 °C from that measured by the foil type thermocouple used for calibration. Therefore, the uncertainty associated with wall temperature is estimated to be less than 0.3 °C. Consequently, the uncertainties for the effective heat transfer coefficient and Nusselt number (Nu_e) are estimated to be less than 3.0%.

4. Numerical simulation

Geometric complexity in conjunction with rotating environment inevitably limits experimental access into detailed thermo-fluidic characteristics, especially for cross-drilled brake disc. To facilitate a comprehensive comparison between the two brake discs, a series of three-dimensional (3D) steady-state as well as transient simulations are conducted for both brake discs using a commercial code ANSYS 14.5.

4.1. Computational domain and boundary conditions

The numerical model for a brake disc rotating in ambient air is schematically shown in Fig. 4(a). According to the geometric periodicity of the brake disc and the induced flow field (with buoyancy neglected), only 1/21 of the whole domain is simulated. The axial and radial dimensions of the fluid domain are separately $7(H_v + 2t_r)$ and $2R_{ro}$, which are large enough to eliminate the effects of boundaries on flow and heat transfer nearby the brake disc [27,28].

To simulate electrical or frictional heating, a volumetric heat source with constant intensity is specified in the heat source domains attached to the rubbing discs. The thickness and inner/outer radii of these domains are identical to those of the Inconel layer in the heating pad. The generated thermal energy is transferred to both sides of these domains, representing well the situation during experiments and actual braking.

The Perspex knuckle is excluded due to its low thermal conductivity while the knuckle walls are set to be no-slip and adiabatic walls. Rotational periodic boundary conditions are applied to periodic surface pairs of all domains. For the upper, lower and outer boundaries of the fluid domain in Fig. 4(a), an opening condition with zero gauge pressure, atmospheric static temperature and low (i.e., 1.0%) turbulence intensity is applied in an inertial coordinate system. The specified pressure acts as total pressure and static pressure for inflow and outflow, respectively [29]. Absolute flow direction is set to be normal to these boundaries. Given that the magnitude of absolute velocity far away from the brake disc is approximately zero, the opening condition is a reasonable approximation of the complex real situation. In consideration of thermal resistances induced by Kapton films and double-sided tape in the experiment, thermal contact resistances are added at interfaces between the heat source domains and other domains to validate the numerical model. However, these resistances are removed for frictional heating simulation. For other interfaces between the solid and fluid domains, no-slip condition is adopted for fluid flow while conservative interface flux condition is used for heat transfer.

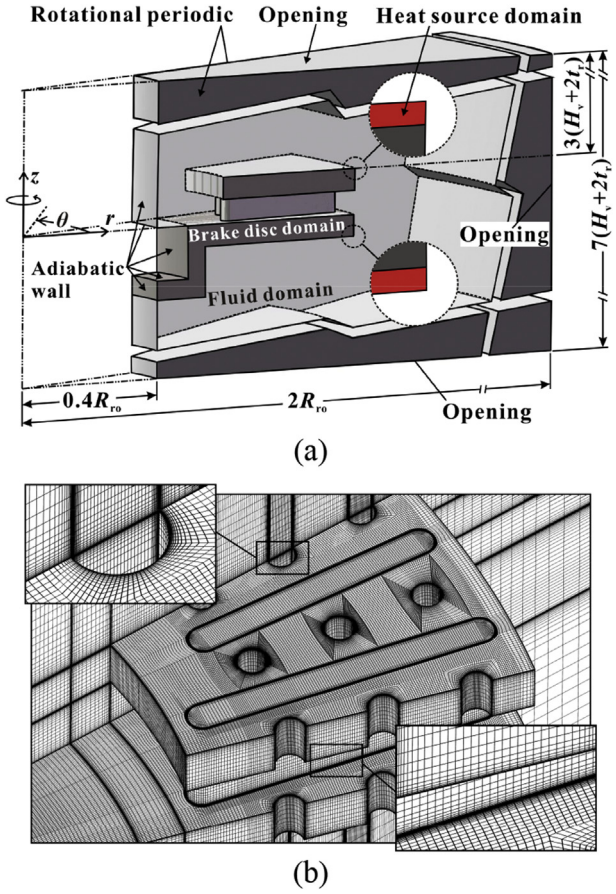

Fig. 4. Details of 3D numerical model: (a) computational domain and boundary conditions; (b) representative mesh.

For transient simulation, the fluid domain is excluded to save computation time. Instead, local heat transfer coefficient (h) and reference temperature (T_a) are specified for all solid walls. Herein, the local heat transfer coefficient is obtained from steady-state flow and conjugate heat transfer solution, defined as:

$$h(r,\theta,z) = \frac{q''(r,\theta,z)}{T(r,\theta,z) - T_a} \tag{4}$$

where q" and T are local heat flux effusing the wall and wall temperature, respectively.

4.2. Numerical methods

A multi-block structured mesh incorporating fully hexahedral elements is generated by ANSYS ICEM CFD 14.5 in all domains, as shown in Fig. 4(b). Fine mesh is generated near all no-slip walls to resolve the boundary layers. To this end, the height of the first layer elements adjacent to the solid walls is set to be ~0.01 mm, followed by smooth transition to relatively coarse mesh away from the walls. One-to-one match of nodes is ensured for periodic faces to eliminate any interpolation error.

Both steady-state and transient simulations are performed using ANSYS CFX 14.5 based on the finite volume method and the time marching algorithm. First, the steady-state flow and conjugate heat transfer problem for all domains is solved in a non-inertial reference frame that rotates at an angular velocity identical to that of the brake disc. The fluid (air) is assumed to be incompressible and has constant thermo-physical properties based on ambient pressure and temperature. The shear stress transport (SST) model [30] incorporating a dimensionless wall distance (y^+) less than 1.0 is adopted to obtain turbulent viscosity and Prandtl number, due to its good performance for rotating flows subjected to adverse pressure gradient as those associated with centrifugal compressors [31] and ventilated brake discs [27,32]. The complete governing equations are not shown here for brevity but can be found in Ref. [29]. The high resolution scheme is selected to discretize the advection terms in the governing equations to reduce numerical error. Subsequently, transient heat conduction in the solid domains is solved, where the second order backward Euler scheme is selected to discretize the transient term in the governing equation.

4.3. Mesh and time step independence tests

Mesh sensitivity is examined for both brake discs at $N = 1000$ RPM. For the standard brake disc, three meshes with 2,125,347, 3,200,649 and 5,029,674 elements are considered. For the cross-drilled brake disc, however, three finer meshes with 5,510,368, 9,542,252 and 13,050,380 elements are used in order to capture more complex flow field induced by the holes. For both brake discs, the area-averaged effective Nusselt numbers obtained with the last two meshes show a discrepancy less than 0.8%, which is acceptable. Therefore, for effectiveness of computational cost, meshes with 3,200,649 and 9,542,252 elements are used in subsequent simulations for the standard and cross-drilled brake discs, respectively.

For transient simulation, the effect of time step on area-averaged rubbing surface temperature of the inboard disc is examined at 800 RPM. Each complete transient simulation with a span of 3600 s is divided into two processes experiencing 20 s and 3580 s, respectively. In the numerical tests, time steps of 0.1 s and 1 s are adopted for the first process, whereas time steps of 1 s and 10 s are adopted for the other process. Numerical results obtained with the two different time steps show a maximum deviation less than 0.5%. Therefore, time steps of 1 s and 10 s are used for the first

20 s and the following 3580 s of the transient simulation, respectively.

5. Discussion of results

5.1. Validation of numerical model

Before comparisons between standard and cross-drilled brake discs made of cast iron are made, the numerical model detailed in the previous section is validated by experimental data obtained from the present stainless steel brake disc. Fig. 5 compares the numerically predicted variation of area-averaged rubbing surface temperature ($T_{rs,\,m}$) with time (t) with that measured experimentally. The numerical results agree well with the experimental ones, with a maximum discrepancy of 5.4%.

For further validation, steady-state local heat transfer characteristics of the brake disc obtained from experiment and numerical simulation are compared. Fig. 6 presents the localized distributions of effective Nusselt number (Nu_e) calculated according to Eqs. (2) and (3) at 800 RPM. Both contours of Fig. 6(a) qualitatively indicate an approximately isotropic distribution in the azimuth direction. Again, as quantified in Fig. 6(b), good agreement between experimental and numerical results is achieved, with a maximum deviation of 6.0%.

Finally, the area-averaged effective Nusselt number ($Nu_{e,\,m}$) calculated from a series of contours as those in Fig. 6(a) is plotted in Fig. 7 as a function of rotational Reynolds number (Re). The experimental and numerical data sets of Fig. 7 both demonstrate that the Nusselt number increases with increasing Reynolds number, exhibiting a maximum discrepancy of 9.0% at $N = 200$ RPM. For the present experiments, it is estimated that thermal radiation from black paint accounts for 10.4% (at 200 RPM) to 3.5% (at 1000 RPM) of total heat transfer. At lower rotational speeds, radiation heat transfer from the ventilated channel walls to the surroundings and natural convection [33] are more significant. The contributions of these two factors to overall heat transfer, however, are not subtracted in Eq. (3) as they are difficult to estimate. Therefore, in Fig. 7, the largest deviation between experiment and numerical simulation occurs at the lowest rotational speed.

In summary, for both local and overall heat transfer characteristics, the present numerical simulation results agree reasonably well with experimental measurements. Therefore, the numerical model is suitable for subsequent comparative investigations.

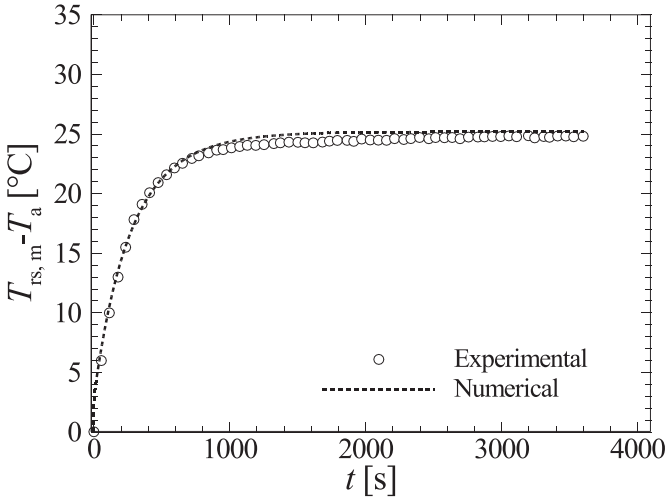

Fig. 5. Comparison of measured and numerically predicted transient evolutions of area-averaged rubbing surface temperature at 800 RPM.

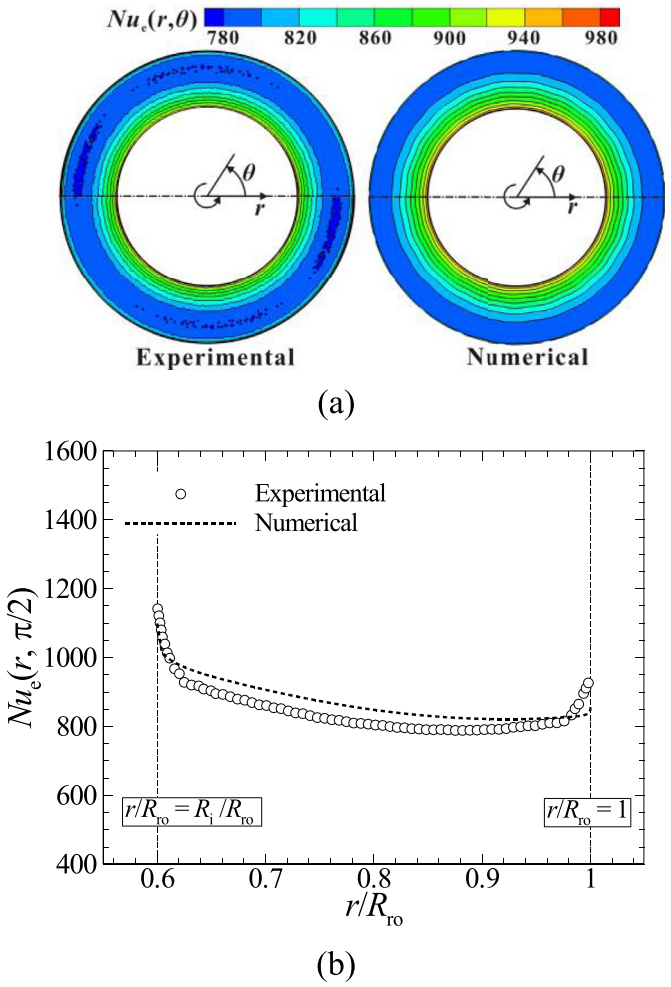

Fig. 6. Comparison of measured and numerically predicted effective Nusselt number distributions on rubbing surface at 800 RPM: (a) two-dimensional contour; (b) radial profile at $\theta = \pi/2$ extracted from (a).

5.2. Modification of fluid flow by cross-drilled holes

For a ventilated brake disc, convective heat transfer via internal and external cooling flows driven separately by rotating heat dissipation elements and rubbing discs is the dominant heat dissipation mechanism [34]. To improve brake disc cooling, modification of these flow patterns has attracted much attention, as realized by cross-drilled holes in the present study. Firstly, as basis of local heat transfer pattern on brake disc surface, the effects of cross-drilled holes on fluid flow are discussed. The results presented are for $N = 400$ RPM and analyzed in a non-inertial reference frame rotating at an angular velocity identical to that of the brake disc. For clarity, special focus is placed upon fluid flow associated with the inboard disc, as similar flow characteristics are observed for the outboard disc and at other rotational speeds.

5.2.1. Initiation of flow through cross-drilled holes

Fig. 8 presents an overview of 3D flow patterns (as indicated by streamlines), revealing both the common and distinct characteristics between the brake discs. When the brake disc starts to rotate, the originally stationary air in the ventilated channel is driven radially outwards by centrifugal force, lowering hence the static pressure at the ventilated channel inlet. Consequently, a pressure driven flow from ambient into the ventilated channel occurs. Part of

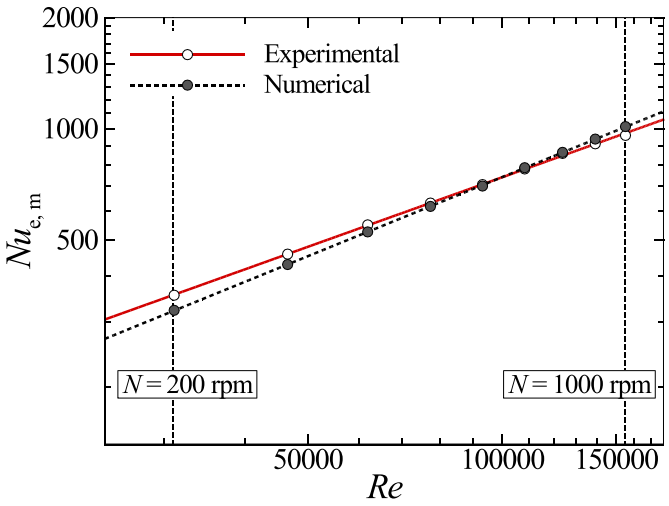

Fig. 7. Comparison of area-averaged effective Nusselt numbers obtained from experiment and numerical simulation at selected rotational Reynolds numbers.

the fluid is directly sucked into the ventilated channel as highlighted by the blue streamlines, while some other fluid wipes the inner rim surface of the inboard disc as highlighted by the red streamlines. As a result of the Coriolis force, the flow follows a spiral path. These flow patterns are in good agreement with the PIV and helium bubble visualization results presented in Refs. [35,36].

In particular for the standard brake disc, the external flow driven by the rotating disc wipes the rubbing surface till the outer rim of the disc, as highlighted by the black streamlines in Fig. 8(a). For the cross-drilled brake disc, however, fluid wiping the rubbing surface finally enters the ventilated channel through the cross-drilled holes, as marked by the black streamlines in Fig. 8(b). As further detailed in Fig. 9, the surface streamlines on three cylindrical cross-sections (at $r = R_{h1}$, R_{h2} and R_{h3}) clearly distinguish the unique flow characteristics between the two different brake discs. It is seen from Fig. 9 that the static pressure in the ventilated channel is generally lower than that nearby the rubbing surface. Such an axial pressure difference drives the fluid to turn its flow direction into the cross-drilled holes.

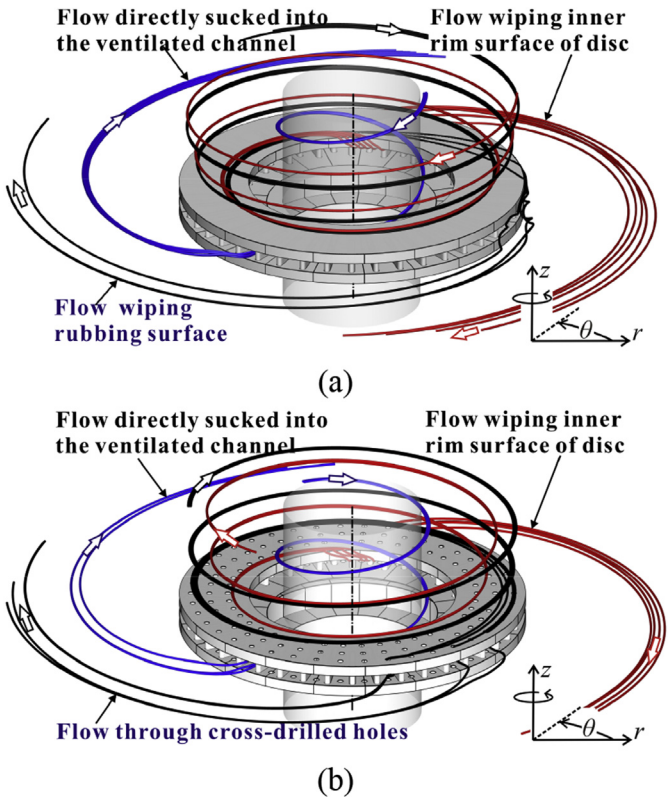

Fig. 8. Three-dimensional streamlines summarizing overall flow patterns for the (a) standard and (b) cross-drilled ventilated brake discs.

5.2.2. Effect of through-hole flow on external flow

Cross-drilled holes act as "sinks" to external flow, imposing two significant effects on boundary layer flow over the rubbing surface. First, fluid closer to the disc wall has a lower momentum component parallel to the wall. In the presence of axial pressure gradient (along the z-axis), fluid passing by the upstream lip of the holes can easily change its flow direction and then enters the holes; see

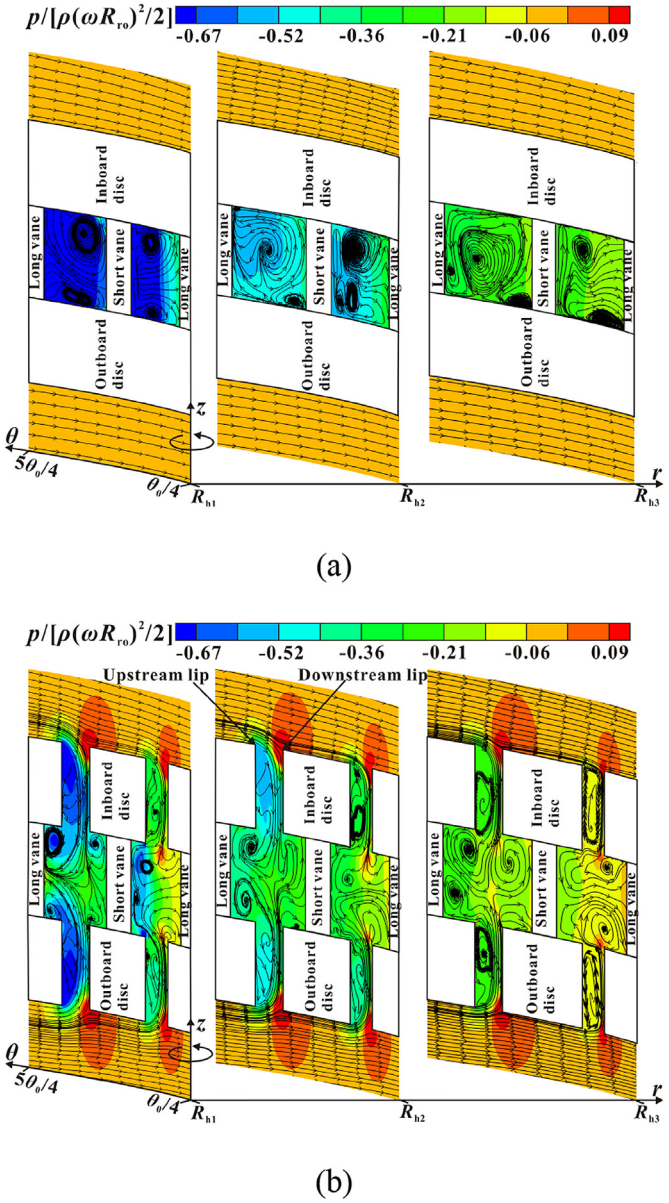

Fig. 9. Surface streamlines and static pressure (p) distributions on three cylindrical cross-sections at $r = R_{h1}$, R_{h2} and R_{h3} for (a) standard and (b) cross-drilled brake discs.

Fig. 9(b). As a result, the thickness of flow boundary layer circumferentially downstream each hole is diminished relative to that of the standard brake disc. Second, flow impingement onto the downstream lip of each hole substantially increases local static pressure, while suction of fluid nearby the upstream lip of each hole into the ventilated channel lowers local static pressure, as clearly revealed by Fig. 9(b). Consequently, in contrast to circumferentially isotropic pressure distribution for the standard brake disc, an azimuth pressure difference between the downstream and upstream lips of two neighboring holes exists; see Fig. 10(a). Such a pressure difference tends to accelerate fluid flow inside the boundary layer for the cross-drilled brake disc.

For both brake discs, Fig. 10(b) presents the velocity distribution on an r-θ plane 0.1 mm over the rubbing surface. A circumferentially isotropic distribution is observable for the standard brake disc. For the cross-drilled brake disc, however, substantially accelerated flow is evident within the radial spans of cross-drilled holes due to the aforementioned effects. For both brake discs, the wall shear stress distributions that dominate local heat transfer on rubbing surfaces show consistent patterns with the velocity distributions of Fig. 10(b), and hence are not presented here for brevity.

5.2.3. Effect of through-hole flow on internal flow

In addition to altering external flow over the rubbing discs, the through-hole flow also modifies fluid flow inside the ventilated channel. As reference, Fig. 11 first characterizes internal flow for the standard brake disc in terms of 3D streamlines. Under the effect of Coriolis force, the flow pre-swirls towards the counter-rotating direction before entering the ventilated channel [35]. Thus the relatively large flow attack angle to each vane causes flow separation at the leading edge of the vane. Additionally, the presence of centrifugal force in conjunction with the diverging nature of internal flow leads to an adverse pressure gradient along the radial direction, as shown in Fig. 9. These two effects induce severe flow recirculation nearby the suction sides of the vanes, as indicated by blue and red streamlines, in contrast to smooth fluid flow nearby the pressure sides of the vanes as marked by green streamlines.

For comparison, Fig. 12 presents the corresponding internal flow characteristics for the cross-drilled brake disc. To demonstrate the bulk flow behavior of air jets issuing from the cross-drilled holes, a large number of streamlines released from the inlet of each hole are elaborately selected. It is evident from Fig. 12 that these air jets feed fluid to the suction sides of the vanes, which suppresses the severe

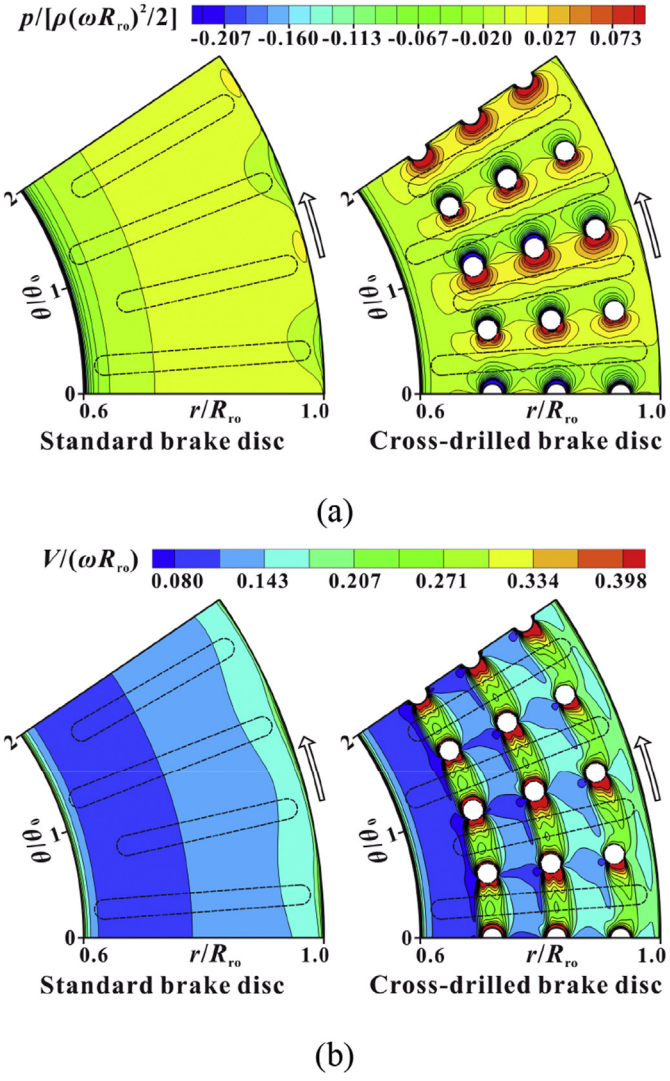

Fig. 10. Comparison of external flow characteristics: (a) static pressure distribution on inboard rubbing surface; (b) velocity magnitude distribution on an r-θ plane 0.1 mm over the rubbing surface.

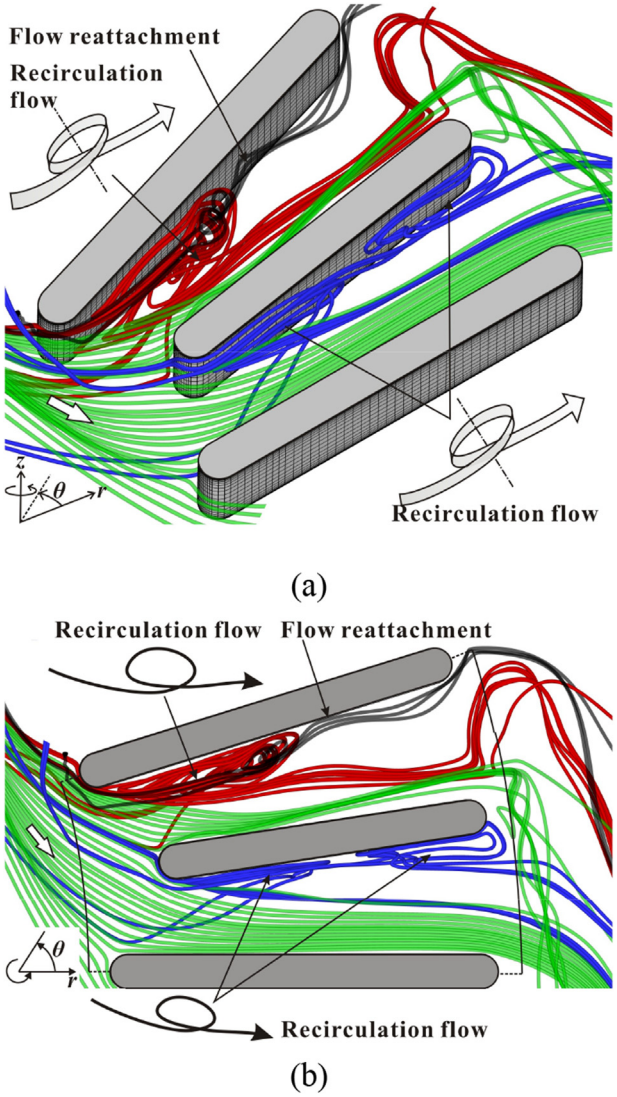

Fig. 11. Internal flow characteristics as indicated by streamlines for standard brake disc: (a) isometric view; (b) top view.

local flow recirculation observed for the standard brake disc (see Fig. 11). In addition, smooth cross flow is observable nearby the pressure sides of the vanes as indicated by green streamlines in Fig. 12.

Cross-drilled holes may be clarified into six different types, as denoted by (I) to (VI) in Fig. 12, which impose distinct effects on internal flow. First, Fig. 12(b) reveals that air jets from holes located at a smaller radius dominate fluid flow nearby the suction sides of the vanes. In particular, fluid from holes (I) and (IV) covers nearly all the suction sides of the vanes, while fluid from holes (III) and (VI) can hardly attach the vane surface. Second, air jets impose more significant blockage to cross flow in passage (A) than that in passage (B), as shown in Fig. 12(b). Finally, air jets into passage (A) first transport fluid to the mid-height plane of the passage and then deflect to the suction side of the long vane, as highlighted in Fig. 12(c). However, upon entering the ventilated channel, air jets into passage (B) deflect immediately to the suction side of the short vane; see Fig. 12(d).

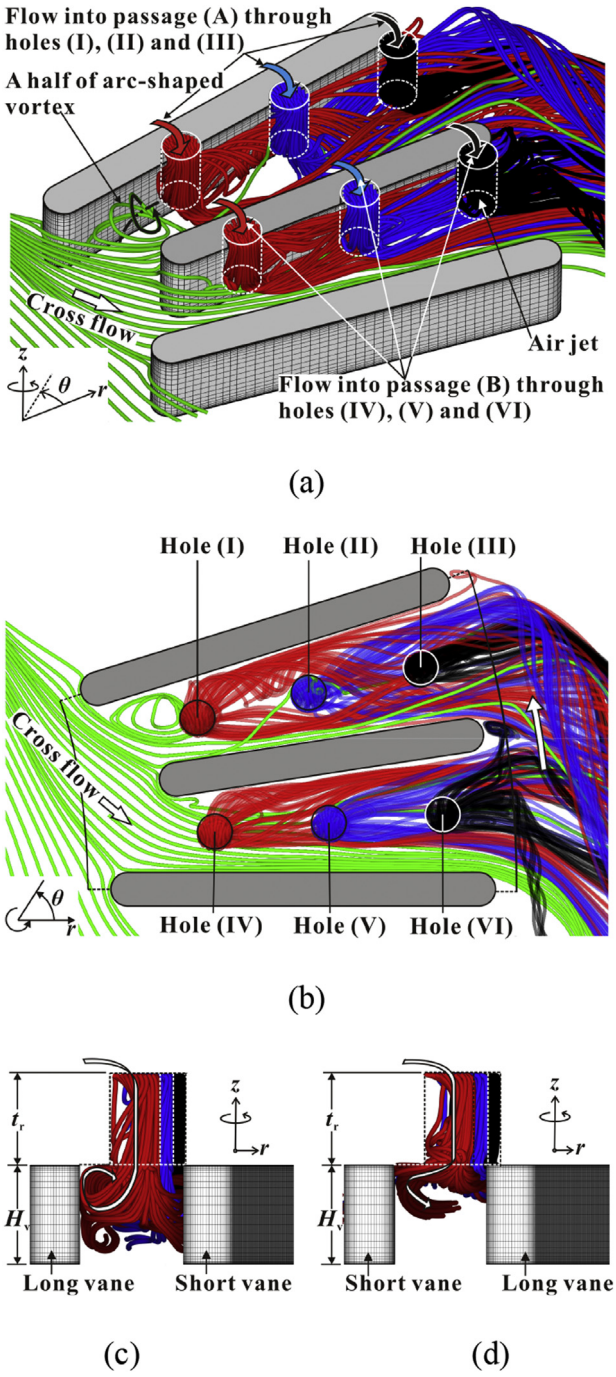

Fig. 12. Internal flow characteristics as indicated by streamlines for cross-drilled brake disc: (a) isometric view; (b) top view; (c) and (d) radial views of air jets in passage (A) and passage (B), respectively.

The modification of internal flow by cross-drilled holes alters the pumping capacity of the brake disc, which in turn affects heat transfer on ventilated channel walls. Fig. 13 presents the normalized mass flow rate calculated with the product of fluid density (ρ), peripheral velocity (ωR_{ro}) and ventilated channel outlet flow area ($2\pi R_{ro} H_v$). The shaded strips represent the radial spans of cross-drilled holes. For the standard brake disc, the inherent pre-swirl of fluid flow towards the counter-rotating direction leads to a 46% lower mass flow rate through passage (A) than that through passage (B); see Fig. 13(a). Once cross-drilled holes are introduced, the smaller cross-flow momentum in conjunction with a larger flow recirculation region (see Fig. 11) in passage (A) enables more air to enter passage (A) through the cross-drilled holes compared with that in passage (B); see Fig. 13(b). Subsequently, the blockage of cross flow by air jets lowers the pumping capacity from the ventilated channel inlet of the cross-drilled brake disc. Finally, Fig. 13(b) reveals that cross-drilled holes located closer to the ventilated channel inlet exhibit higher mass flow rates due to streamwise reduction of the axial pressure gradient, as previously shown in Fig. 9.

Fig. 14 compares velocity distribution on an r-θ plane 0.1 mm away from the inner disc surface of the standard brake disc with that of the cross-drilled brake disc. Nearby the suction sides of the vanes, it is clear that low-momentum flow (due to recirculation) for the standard brake disc is replaced by high-momentum flow (from air jets) for the cross-drilled brake disc. In addition, low-momentum regions are observable downstream the holes, corresponding to wake vortices of air jets in cross flow [37]. Within the remaining part of the region, the velocity magnitude for the cross-drilled brake disc is in general lower than that for the standard brake disc, due mainly to reduced pumping capacity from the ventilated channel inlet; see Fig. 13(a).

5.3. Modification of local heat transfer pattern by cross-drilled holes

As the presence of cross-drilled holes substantially modifies external and internal flows, consider next how the modified flow pattern may affect local heat transfer pattern on brake disc surface, which ultimately dictates the overall cooling performance of the brake disc. For consistency, only local heat transfer results obtained at $N = 400$ RPM for the inboard disc are presented, as similar characteristics are observed for the outboard disc and at other rotational speeds. Henceforth, the local Nusselt number (Nu) is defined as:

$$Nu(r,\theta,z) = \frac{R_{ro} h(r,\theta,z)}{k} \tag{5}$$

where the thermal conductivity of air is based on ambient air temperature and pressure, and the local heat transfer coefficient (h) is previously defined in Eq. (4).

5.3.1. Local heat transfer on rubbing surface

Fig. 15(a) presents the distribution of local Nusselt number on the inboard rubbing surface for both brake disc types. For the standard disc, the approximately isotropic velocity distribution as

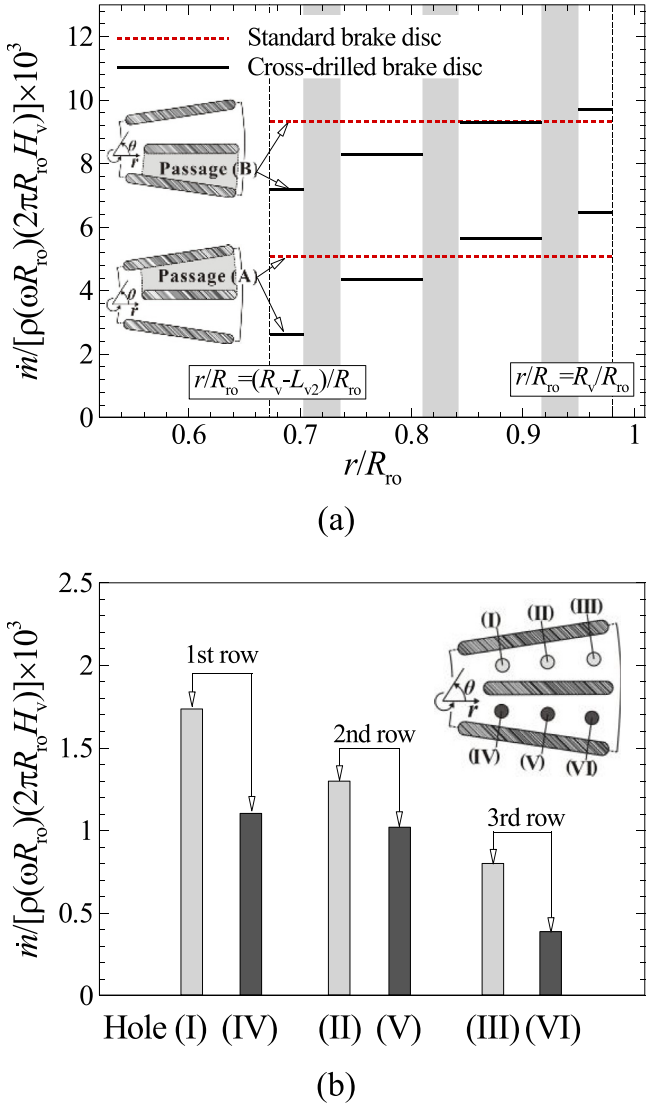

Fig. 13. Pumping capacity comparison between standard and cross-drilled brake discs: (a) mass flow rates through passages (A) and (B); (b) mass flow rates through cross-drilled holes extracted from (a).

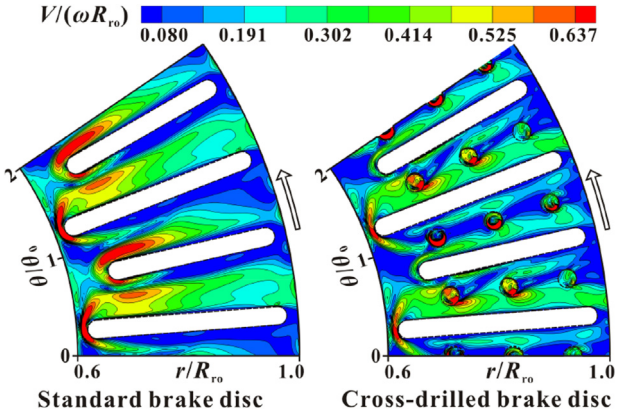

Fig. 14. Velocity magnitude distribution on an r-θ plane 0.1 mm away from inner surface of inboard disc: comparison between standard and cross-drilled brake discs.

shown in Fig. 10(b) leads to a circumferentially isotropic heat transfer distribution. The Nusselt number remains nearly constant within most of the radial span, whereas substantially higher heat transfer is observed nearby the inner and outer rims of the disc, which is attributed to the entrainment effects of inflow and outflow through the ventilated channel. The cross-drilled disc, however, exhibits an anisotropic heat transfer pattern. Substantially enhanced local heat transfer is evident within the radial spans of the cross-drilled holes, corresponding to accelerated boundary layer flow as shown in Fig. 10(b). The impingent of flow onto the downstream lip of each hole leads to the peak of local heat transfer; see Fig. 15(a). Circumferentially downstream each hole, the local heat transfer gradually diminishes due to development of thermal boundary layer and flow deceleration.

For quantitative comparison, Fig. 15(b) presents the profiles of azimuthally averaged Nusselt number in the radial direction, with the radial span of each hole marked as shaded strip. Relative to the standard disc, the Nusselt number nearby the first row of holes is augmented by up to 250%. The relative enhancement is reduced to 230% and 160% nearby the second and third rows of holes, respectively. Such gradual decrease of relative heat transfer

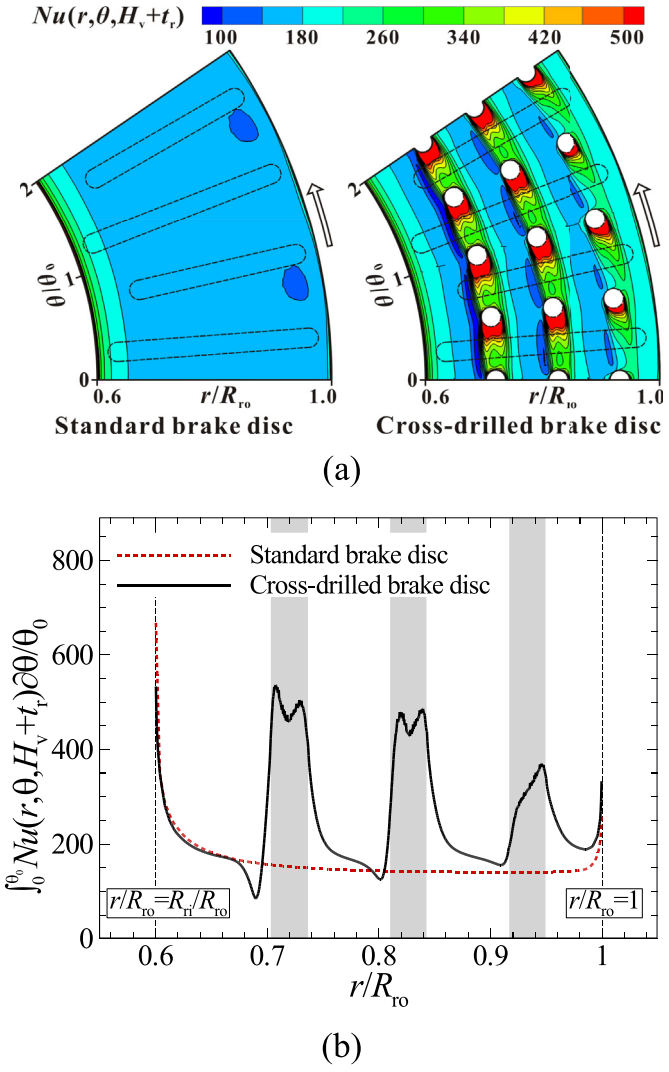

Fig. 15. Comparison of local heat transfer characteristics on inboard rubbing surface: (a) contour of Nusselt number; (b) variation of azimuthally averaged Nusselt number along radial direction.

enhancement is consistent with the gradual reduction of mass flow rate through these holes, as shown previously in Fig. 13(b).

5.3.2. Local heat transfer on inner disc surface

Fig. 16(a) presents local heat transfer distribution on the inner surface of the inboard disc, which exhibits consistent pattern with the velocity distribution of Fig. 14. For both discs, a similar heat transfer pattern is seen nearby the leading edges and pressure sides of the vanes, which is dominated by fluid flow entering from the ventilated channel inlet. For the cross-drilled disc, the area of the U-shaped high heat transfer region around each vane is smaller than that for the standard disc, especially around the short vane. Blockage of cross flow by the air jets and reduced pumping capacity from the ventilated channel inlet (see Fig. 13(a)) are responsible for such deteriorated local heat transfer. For the cross-drilled disc, in particular, improved heat transfer occurs nearby the suction sides of the vanes, due to feeding of fluid by the air jets. Downstream the cross-drilled holes, the wake vortices downstream the air jets in cross flow lead to poor local heat transfer.

For quantitative comparison, Fig. 16(b) presents the variation of azimuthally averaged Nusselt number along the radial direction.

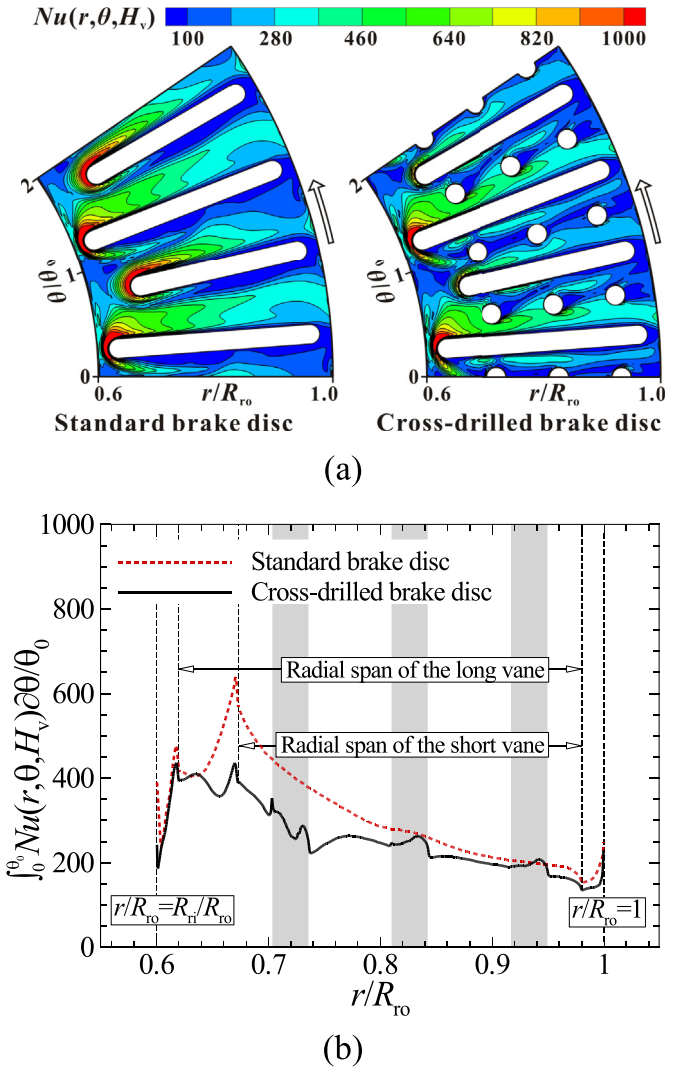

Fig. 16. Comparison of local heat transfer characteristics on inner surface of inboard disc: (a) contour of Nusselt number; (b) variation of azimuthally averaged Nusselt number along radial direction.

The shaded strips denote the radial spans of the cross-drilled holes. For the standard disc, flow contraction due to blockage of flow area by the vanes leads to several peaks of the Nusselt number, occurring at the leading edges of the vanes. Downstream the leading edge of the short vane, the Nusselt number gradually decreases due to flow divergence and development of thermal boundary layer. A similar radial trend is present for the cross-drilled disc. Within the full radial span of the inboard disc, it is clear from Fig. 16(b) that heat transfer is deteriorated by the introduction of cross-drilled holes. For example, between the leading edge of the short vane and the first row of holes, the Nusselt number is reduced by about 30%. The deterioration gradually weakens along the radial direction, due to the gradual feeding of fluid by the air jets into the cross flow.

5.3.3. Local heat transfer on vane surface

Fig. 17 presents local heat transfer distribution on unfolded vane surfaces, where the dashed lines and shaded strips mark the azimuth projections of cross-drilled holes onto the vanes. Herein, P_v is the perimeter of the vane cross-section; and s denotes the local curvilinear coordinate originating from the leading edge of the vane as illustrated in Fig. 17(b) and (c).

For both brake discs, on the pressure sides of the vanes, the Nusselt number peaks nearby the leading edge and then gradually decreases along the negative s-axis due to flow deceleration and thermal boundary layer development. On the suction sides of the vanes for the standard brake disc, the Nusselt number is substantially lower than that on the pressure sides due to severe local flow recirculation. In contrast, on the suction sides of the vanes for the cross-drilled brake disc, substantial local heat transfer enhancement is achieved within regions washed by the air jets. As previously mentioned, air jets into passage (A) can penetrate to the mid-height plane of the ventilated channel and then impinge onto the suction side of the long vane; see Fig. 12(c). Therefore, the high heat transfer region downstream the first row of holes is located at the central region of the long vane. The area of this high heat transfer region gradually decreases along streamwise direction, due to the subdued effect of air jets further downstream. In addition, upon entering the ventilated channel, the air jets into passage (B) deflect immediately to the suction side of the short vane; see Fig. 12(d). Consequently, there exist two separated high heat transfer regions adjacent to the inboard and outboard discs, respectively.

For quantitative comparison, Fig. 17(b) and (c) present the variation of axially averaged Nusselt number as a function of s for long and short vanes, respectively. The decreased approaching velocity ahead of the vanes (see Fig. 13(a)) reduces local heat transfer at the leading edges by up to 25%. In contrast, local heat transfer on the pressure sides of the vanes remains almost unchanged. The impingement of air jets onto the suction sides of the vanes substantially enhances local heat transfer, up to 7 times and 3 times for the long vane and short vane, respectively.

5.3.4. Local heat transfer on surface of hole

While cross-drilled holes decrease the rubbing surface and inner surface area of the disc, they also introduce additional heat transfer area, i.e., surfaces of the holes, washed by through-hole flow. Local heat transfer characteristics on such unique surfaces are presented in Fig. 18 for the cross-drilled brake disc. Local heat transfer on the pressure side of the hole is dominated by smooth high speed flow, while that on the suction side is dominated by severe flow recirculation as revealed by streamlines presented in Figs. 9(b), 12(c) and 12(d). Therefore, much higher Nusselt number is achieved at the pressure side as shown in Fig. 18(a). As quantified in Fig. 18(b), cross-drilled holes corresponding to passage (A), i.e., holes (I)–(III), exhibit higher heat transfer than those

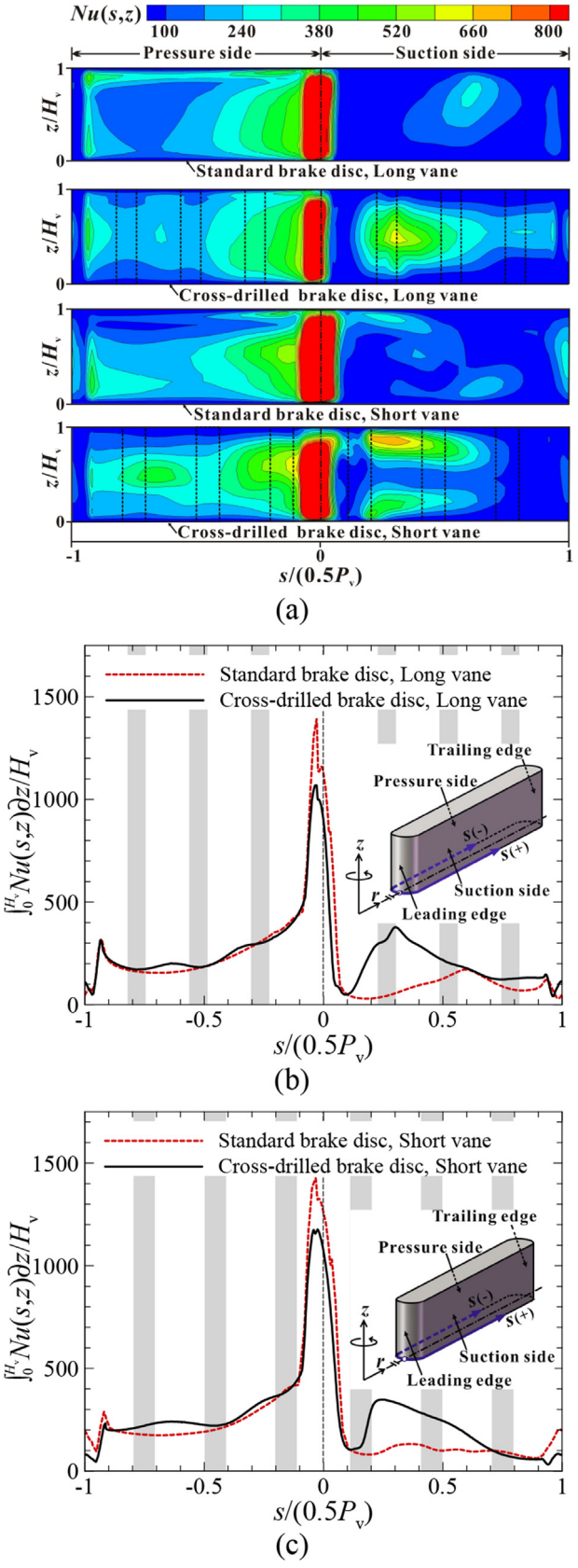

Fig. 17. Comparison of local heat transfer characteristics on unfolded vane surfaces: (a) contour of Nusselt number; (b) and (c) variation of axially averaged Nusselt number as a function of local curvilinear coordinate (s) for long vane and short vane, respectively.

corresponding to passage (B), i.e., holes (IV)–(VI). Further, holes placed closer to the ventilated channel inlet provide better heat transfer. Such trends are consistent with those exhibited by mass flow rates as shown in Fig. 13(b).

5.4. Overall heat transfer enhancement

It has been demonstrated in Section 5.3 that flow through cross-drilled holes improves heat transfer on both the rubbing and vane surfaces but deteriorates heat transfer on the inner surface of the rubbing disc. Moreover, the through-hole flow removes heat from the surfaces of the holes. How these mutually conflicting mechanisms would affect the overall cooling performance of a cross-drilled brake disc is examined in this section.

5.4.1. Transient and steady-state cooling performance

Depending on brake mode such as short-time emergency braking and long-time downhill braking, heat transfer associated with a brake disc can be transient or steady-state. To characterize

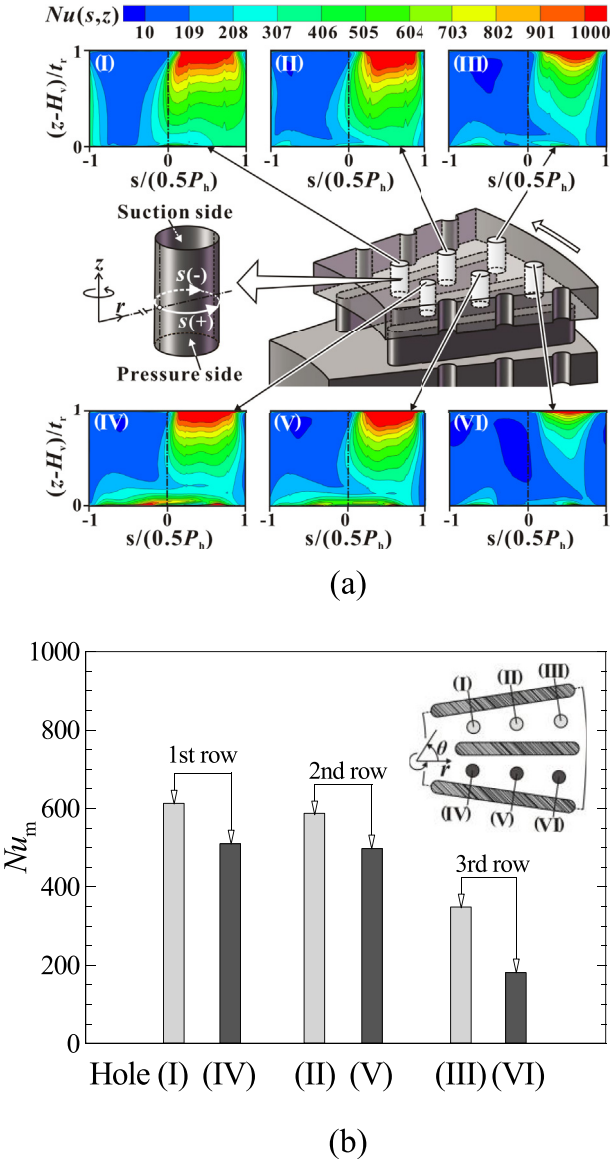

Fig. 18. Local heat transfer characteristics on surfaces of cross-drilled holes: (a) contours of Nusselt number; (b) area-averaged Nusselt numbers obtained from (a).

and compare the cooling performances of the two brake discs experiencing these two distinctive heat transfer processes, extended downhill braking at a typical vehicle speed of 50 km/h (i.e., 400 RPM) is considered. For a typical passenger vehicle with a weight of 1500 kg descending a 7% gradient (i.e., 4°) slope, the total braking power is estimated to be 14.26 kW [38]. It has been reported that nearly 80% of the brake load is imposed on the front axle of the vehicle [38]. Further, about 90% of the frictional heat is transferred to the brake discs [2]. Ultimately, the frictional power for each front brake disc is calculated to be 5.13 kW. Such a power input in conjunction with an ambient air temperature of 20 °C is used in the numerical simulations.

Fig. 19(a) compares the temperature fields in both brake discs at $t = 3600$ s. While the highest temperature is located at the rubbing surface due to direct heating, the lowest temperature occurs at the hub that acts as a fin to the outboard disc. Relative to the standard brake disc, the results of Fig. 19(a) demonstrate clearly that the cross-drilled brake disc has substantially lower temperature at arbitrary position.

To quantify the relative merits of the brake discs during the full transient process, the evolution of area-averaged temperature on the inboard rubbing surface is extracted from a series of temperature fields as those in Fig. 19(a) and plotted in Fig. 19(b). At the very beginning of the transient process, the temperature difference between the brake disc and cooling air is low, implying negligible convective heat dissipation. Therefore, the thermal capacity of the rubbing disc dominates disc temperature [16]. The introduction of cross-drilled holes reduces the thermal capacity of the inboard rubbing disc by 5.47%. As a result, the cross-drilled disc exhibits up to 5.2% higher operating temperature when $t < 110$ s, as highlighted in Fig. 19(c). As the process of braking continues, the cross-drilled disc exhibits increased superiority. Eventually, when heat transfer reaches steady-state, the operating temperature of the cross-drilled disc is 23% (i.e., 141 °C) lower than that of the standard disc.

The steady-state cooling performances of the two brake discs at selected rotational speeds are quantified and compared in Fig. 20. To facilitate the comparison, a unified overall Nusselt number ($Nu_{overall}$) is used for both brake discs, defined as:

$$Nu_{overall} = \frac{R_{ro}}{k}\frac{(0.5Q_t)/A_{ref}}{T_{rs,m} - T_a} \tag{6}$$

where Q_t is the total frictional power input into each brake disc, and the reference area (A_{ref}) is equal to $\pi(R_{ro}^2 - R_{ri}^2)$. As shown in Fig. 20, the Nusselt number increases with increasing rotational Reynolds number. From 200 RPM to 1000 RPM, the overall Nusselt number of the cross-drilled disc is 22–27% higher than that of the standard one.

5.4.2. Quantification of heat transfer enhancement mechanisms

Next, the contribution of each mechanism to overall heat transfer enhancement is quantified. For both brake discs, the present numerical results reveal that the heat transfer rate through the mid-height cross-section of the vanes is less than 1% of total power input into each rubbing disc. Henceforth, only the system consisting of the inboard rubbing disc and half of the vanes is considered for brevity.

By energy balance of the selected system, the overall Nusselt number defined in Eq. (6) may be decomposed as:

$$\left(Nu_{overall} = \frac{R_{ro}}{k}\frac{Q_{rs} + Q_{is} + Q_{vs} + Q_{irs} + Q_{ors}}{A_{ref}(T_{rs,m} - T_a)}\right)_{Standard} \tag{7a}$$

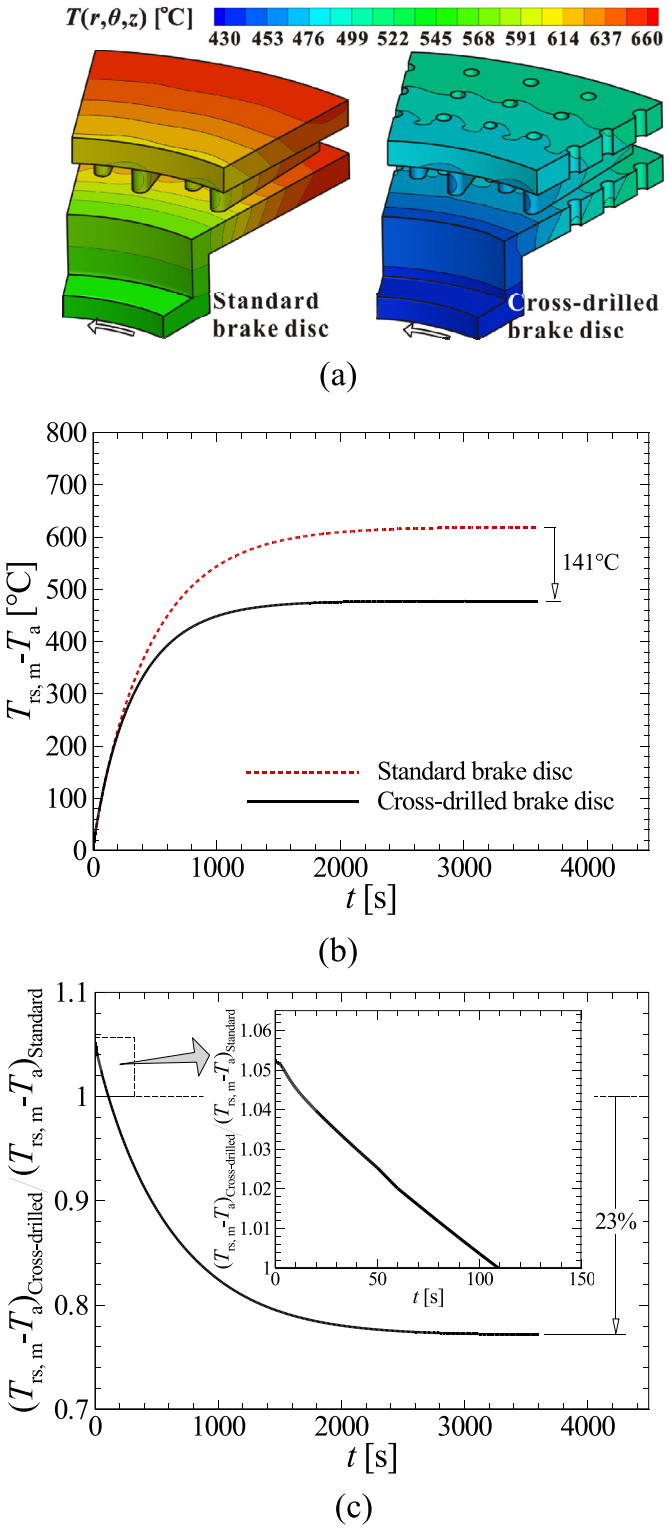

Fig. 19. Transient thermal behaviors of brake discs during extended downhill braking at 400 RPM: (a) representative temperature field at $t = 3600$ s; (b) evolution of area-averaged temperature on inboard rubbing surface; (c) operating temperature ratio.

$$\left(Nu_{overall} = \frac{R_{ro}}{k}\frac{Q_{rs} + Q_{is} + Q_{vs} + Q_{irs} + Q_{ors} + Q_{hs}}{A_{ref}(T_{rs,m} - T_a)}\right)_{Cross-drilled} \tag{7b}$$

where Q is the heat transfer rate; subscripts "rs", "is", "irs" and "ors" denote the rubbing surface, inner surface, inner rim surface and outer rim surface of the inboard disc, respectively; subscripts "vs" and "hs" denote the vane surface and hole surface, respectively; and subscript "m" denotes the area-averaged value.

In Eq. (7), each term corresponds to a specific surface, e.g., inner surface (IS) of the inboard disc, and can be equivalently transformed as:

$$\frac{R_{ro}}{k}\frac{Q_{is}}{A_{ref}(T_{rs,m}-T_a)}=\frac{R_{ro}}{k}\frac{Q_{is}}{A_{is}(T_{is,m}-T_a)}\frac{T_{is,m}-T_a}{T_{rs,m}-T_a}\frac{A_{is}}{A_{ref}} \tag{8}$$

The second term on the right-hand side of Eq. (8) can be further expressed as:

$$\frac{Q_{is}}{A_{is}(T_{is,m}-T_a)}=\frac{\int_{IS}[T_{is}(r,\theta,z)-T_a]h_{is}(r,\theta,z)dA}{\int_{IS}[T_{is}(r,\theta,z)-T_a]dA} \tag{9}$$

$$C_{1,is}=A_{is}\big/A_{ref} \tag{11a}$$

$$C_{2,is}=\left(\frac{T_{is,m}-T_a}{T_{rs,m}-T_a}\right)\left\{\frac{\int_{IS}[T_{is}(r,\theta,z)-T_a]h_{is}(r,\theta,z)dA}{\int_{IS}[T_{is}(r,\theta,z)-T_a]dA}\frac{1}{h_{is,m}}\right\} \tag{11b}$$

$C_{1,\,is}$ represents the contribution of heat transfer area while $C_{2,\,is}$ signifies the effect of material thermal resistance, approaching 1.0 when highly conductive material is used.

Similar derivations as Eqs. 8–11 can be made for all terms appearing in Eq. (7). Consequently, the overall Nusselt numbers for the standard and cross-drilled brake discs can eventually be expressed as:

$$(Nu_{overall}=C_{1,is}C_{2,is}Nu_{is,m}+C_{1,rs}C_{2,rs}Nu_{rs,m}+C_{1,vs}C_{2,vs}Nu_{vs,m}+C_{1,irs}C_{2,irs}Nu_{irs,m}+C_{1,ors}C_{2,ors}Nu_{ors,m})_{Standard} \tag{12a}$$

$$(Nu_{overall}=C_{1,is}C_{2,is}Nu_{is,m}+C_{1,rs}C_{2,rs}Nu_{rs,m}+C_{1,vs}C_{2,vs}Nu_{vs,m}+C_{1,irs}C_{2,irs}Nu_{irs,m}+C_{1,ors}C_{2,ors}Nu_{ors,m}+C_{1,hs}C_{2,hs}Nu_{hs,m})_{Cross-drilled} \tag{12b}$$

Upon substituting Eq. (9) into Eq. (8), the contribution of the inner disc surface to the overall Nusselt number can be quantified in a simple form, as:

$$\frac{R_{ro}}{k}\frac{Q_{is}}{A_{ref}(T_{rs,m}-T_a)}=C_{1,is}C_{2,is}Nu_{is,m} \tag{10}$$

where the coefficients $C_{1,\,is}$ and $C_{2,\,is}$ are given by:

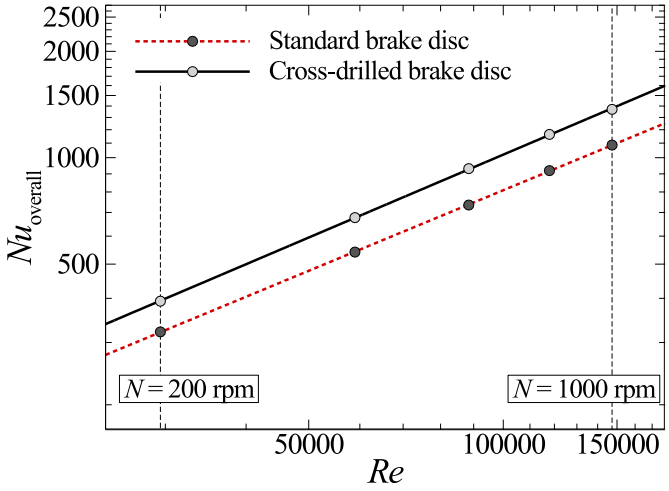

Fig. 20. Comparison of steady-state cooling performance at selected rotational Reynolds numbers.

Subsequently, the contribution of modified heat transfer on a specific surface (e.g., inner disc surface) to overall heat transfer enhancement can be quantified as:

$$\eta_{is}=\frac{(C_{1,is}C_{2,is}Nu_{is,m})_{Corss-drilled}-(C_{1,is}C_{2,is}Nu_{is,m})_{Standard}}{(Nu_{overall})_{Standard}} \tag{13}$$

Table 3 summarizes the values of C_1, C_2 and area-averaged Nusselt number (Nu_m) for the rubbing surface (RS), the inner surface (IS), the inner rim surface (IRS) and the outer rim surface (ORS) of the inboard disc as well as those for the vane surface (VS) and the hole surface (HS). At 400 RPM, the value of coefficient C_2 varies within 0.94–1.0, implying that material thermal resistance is negligible compared with convective resistance. As quantified in Fig. 21 according to Eq. (13), improved heat transfer on the rubbing and vane surfaces by cross-drilled holes augments the overall Nusselt number by 13.2% and 3.6%, respectively. Additional heat removal from the hole surface increases the overall Nusselt number by 19.0%. However, deteriorated heat transfer on the inner surface, inner rim surface and outer rim surface of the inboard disc reduces the overall Nusselt number by 8.9%, 0.8% and 1.1%, respectively. Eventually, with contributions from all the surfaces accounted for, the overall Nusselt number of the cross-drilled brake disc is enhanced by approximately 25% compared with the standard brake disc.

6. Conclusions

A comprehensive comparison of fluid flow and heat transfer behaviors is presented between a standard ventilated brake disc

Table 3
Parameters used for quantification of heat transfer enhancement mechanisms at 400 RPM.

Parameter	Surface of standard brake disc					Surface of cross-drilled brake disc					
	RS	IS	VS	IRS	ORS	RS	IS	VS	IRS	ORS	HS
C_1	1.000	0.773	0.491	0.113	0.188	0.945	0.718	0.491	0.113	0.188	0.394
C_2	0.996	0.960	0.947	0.936	1.002	0.992	0.971	0.958	0.957	1.020	0.947
Nu_m	157.8	298.2	216.7	250.9	183.1	243.6	248.7	256.1	205.4	148.6	274.4

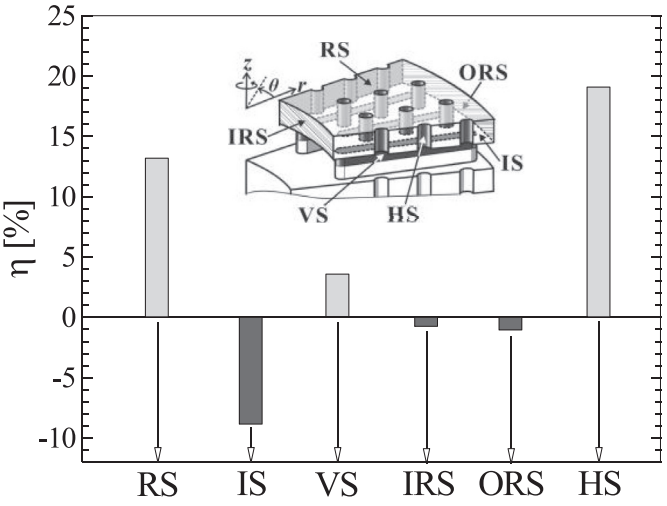

Fig. 21. Contribution of modified heat transfer on various surfaces of the brake disc by cross-drilled holes to overall heat transfer enhancement at 400 RPM.

and a thermally superior cross-drilled ventilated brake disc. Mechanisms underlying the overall heat transfer enhancement by cross-drilled holes are clarified. Conclusions drawn in this study are summarized as follows, which provide beneficial guidance for engineers to further improve brake disc cooling.

(1) Pressure difference drives cooling air into the ventilated channel through cross-drilled holes, causing accelerated boundary layer flow over the rubbing surface. As a result, within the radial spans of the cross-drilled holes, substantially enhanced local heat transfer is achieved. Therefore, further increase of pressure difference is expected to increase the mass flow rate of cooling air through the cross-drilled holes. Correspondingly, local heat transfer on both rubbing surface and surface of holes can be further improved.
(2) Air jets issuing from the cross-drilled holes feed fluid to the suction side of each vane, suppressing local flow recirculation that typically forms for the standard brake disc. Hence, local heat transfer on the suction side of each vane is improved, while local heat transfer on the pressure side remains nearly unchanged. Therefore, facilitating the feeding of fluid by the air jets to suction sides of the vanes is expected to further improve local heat transfer on vane surface.
(3) Blockage of cross flow by air jets reduces the pumping capacity through the ventilated channel inlet and causes a low-momentum wake downstream each jet. Therefore, heat transfer on the inner surface of each rubbing disc is deteriorated. Hence, weakening the blockage effect of the air jets is expected to increase the pumping capacity of the cross-drilled brake disc. Correspondingly, local heat transfer on inner surface of each rubbing disc may be improved.
(4) Within the typical operating range (i.e., 25–124 km/h) of a passenger vehicle, the cross-drilled brake disc exhibits a 22–27% higher steady-state overall Nusselt number than that obtainable by the standard one. Enhanced local heat transfer on the rubbing surface in conjunction with additional heat removal from the surfaces of cross-drilled holes is the dominant mechanism for overall heat transfer enhancement. In addition, cross-drilled holes placed closer to the ventilated channel inlet play a more prominent role in cooling performance enhancement.
(5) According to the above thermo-fluidic mechanisms, placing the cross-drilled holes closer to suction sides of the vanes is expected to further improve local heat transfer on all surfaces of the cross-drilled brake disc. Hence, further enhanced overall cooling performance can be achieved.

Acknowledgements

This research was supported by the National Basic Research Program of China (Grant No.: 2011CB610305), the National 111 Project of China (Grant No.:B06024) and the National Natural Science Foundation of China (Grant Numbers: 51206128 and 51506160).

References

[1] J.E. Hunter, S.S. Cartier, D.J. Temple, R.C. Mason, Brake fluid vaporization as a contribution factor in motor vehicle collisions, SAE Technical Paper No. 980371.
[2] D. Phan, D. Kondyles, Rotor design and analysis: a technique using computational fluid dynamics (CFD) and heat transfer analysis, SAE Technical Paper No. 2003-01-3303.
[3] E. Palmer, R. Mishra, J. Fieldhouse, J. Layfield, Analysis of air flow and heat dissipation from a high performance GT car front brake, SAE Technical Paper No. 2008-01-0820.
[4] M. Pevec, I. Potrc, G. Bombek, D. Vranesevic, Prediction of the cooling factors of a vehicle brake disc and its influence on the results of a thermal numerical simulation, Int. J. Automob. Technol. 13 (5) (2012) 725–733.
[5] K. Lee, Numerical prediction of brake fluid temperature rise during braking and heat soaking, SAE Technical Paper No. 1999-01-0483.
[6] I. Ahmed, P.S. Leung, P.K., Datta, Experimental investigations of disc brake friction, SAE Technical Paper No. 2000-01-2778.
[7] M.H. Cho, S.J. Kim, R.H. Basch, J.W. Fash, H. Jang, Tribological study of gray cast iron with automotive brake linings: the effect of rotor microstructure, Tribol. Int. 36 (7) (2003) 537–545.
[8] S. Anoop, S. Natarajan, S.P. Kumaresh Babu, Analysis of factors influencing dry sliding wear behaviour of Al/SiC_p-brake pad tribosystem, Mater. Des. 30 (9) (2009) 3831–3838.
[9] T. Okamura, H. Yumoto, Fundamental study on thermal behavior of brake discs, SAE Technical Paper No. 2006-01-3203.
[10] T.J. Mackin, S.C. Noe, K.J. Ball, B.C. Bedell, D.P. Bim-Merle, M.C. Bingaman, D.M. Bomleny, G.J. Chemlir, D.B. Clayton, H.A. Evans, R. Gau, J.L. Hart, J.S. Karney, B.P. Kiple, R.C. Kaluga, P. Kung, A.K. Law, D. Lim, R.C. Merema, B.M. Miller, T.R. Miller, T.J. Nielson, T.M. O'Shea, M.T. Olson, H.A. Padilla, B.W. Penner, C. Penny, R.P. Peterson, V.C. Polidoro, A. Raghu, B.R. Resor, B.J. Robinson, D. Schambach, B.D. Snyder, E. Tom, R.R. Tschantz, B.M. Walker, K.E. Wasielewski, T.R. Webb, S.A. Wise, R.S. Yang, R.S. Zimmerman, Thermal cracking in disc brakes, Eng. Fail. Anal. 9 (1) (2002) 63–76.
[11] C.H. Gao, J.M. Huang, X.Z. Lin, X.S. Tang, Stress analysis of thermal fatigue fracture of brake disks based on thermomechanical coupling, ASME J. Tribol. 129 (3) (2007) 536–543.
[12] T.K. Kao, J.W. Richmond, A. Douarre, Brake disc hot spotting and thermal judder: an experimental and finite element study 23 (3–4) (2000) 276–296.
[13] A. Belhocine, M. Bouchetara, Thermal behavior of full and ventilated disc brakes of vehicles, J. Mech. Sci. Technol. 26 (11) (2012) 3643–3652.
[14] T.C. Chatterley, M.P. Macnaughtan, Cast iron brake discs—current position, performance and future trends in Europe, SAE Technical Paper No. 1999-01-0141.

[15] T.H. Thomas, Disc brakes “two years after”, SAE Technical Paper No. 670197.
[16] H.B. Yan, Q.C. Zhang, T.J. Lu, An X-type lattice cored ventilated brake disc with enhanced cooling performance, Int. J. Heat. Mass Transf. 80 (2015) 458–468.
[17] L. Wallis, A Comparison of Bi-directional Disc Brake Rotor Passage Designs (Ph.D. thesis), The University of New South Wales, Sydney, Australia, 2003, pp. 90–98.
[18] D. Antanaitis, A. Rifici, The effect of rotor crossdrilling on brake performance, SAE Technical Paper No. 2006-01-0691.
[19] G. Barigozzi, A. Perdichizzi, P. Pacchiana, R. Goller, Aero-thermal characteristics of an automotive CCM vented brake disc, SAE Technical Paper No. 2005-01-3930.
[20] S.W. Kim, K. Park, S.H. Lee, K.H. Kang, K.T. Lim, Thermophysical properties of automobile metallic brake disc materials, Int. J. Thermophys. 29 (2008) 2179–2188.
[21] Q.C. Zhang, Y.J. Han, C.Q. Chen, T.J. Lu, Ultralight X-type lattice sandwich structure (I): concept, fabrication and experimental characterization, Sci. China Ser. E Technol. Sci. 52 (8) (2009) 2147–2154.
[22] T. Wen, J. Tian, T.J. Lu, D.T. Queheillalt, H.N.G. Wadley, Forced convection in metallic honeycomb structures, Int. J. Heat. Mass Transf. 49 (19) (2006) 3313–3324.
[23] J.N. Sweet, E.P. Roth, M. Moss, Thermal conductivity of Inconel 718 and 304 stainless steel 8 (5) (1987) 593–606.
[24] M.E. Lyall, Heat Transfer from Low Aspect Ratio Pin Fins (Master thesis), Virginia Polytechnic Institute and State University, Blacksburg, VA, 2006, p. 61.
[25] T.L. Bergman, A.S. Lavine, F.P. Incropera, D.P. Dewitt, Fundamentals of Heat and Mass Transfer, seventh ed., John Wiley & Sons Inc., Hoboken, New Jersey, 2011, p. 885.
[26] H.W. Coleman, W.G. Steele, Experimentation, Validation, and Uncertainty Analysis for Engineers, third ed., John Wiley & Sons Inc., Hoboken, New Jersey, 2009.
[27] S.M. Reddy, J.M. Mallikarjuna, V. Ganesan, Flow and heat transfer analysis of a ventilated disc brake rotor using CFD, SAE Technical Paper No. 2008-01-0822.
[28] L. Wallis, E. Leonardi, B. Milton, P. Joseph, Air flow and heat transfer in ventilated disc brake rotors with diamond and tear-drop pillars, Numer. Heat Transf. A Appl. 41 (6–7) (2002) 643–655.
[29] CFX 14.5, ANSYS CFX-Solver Theory Guide, ANSYS Inc., Canonsburg, Pennsylvania, 2012.
[30] F.R. Menter, Two-equation eddy-viscosity turbulence models for engineering applications, AIAA J. 32 (8) (1994) 1598–1605.
[31] L. Mangani, E. Casartelli, S. Mauri, Assessment of various turbulence models in a high pressure ratio centrifugal compressor with an object oriented CFD code, ASME J. Turbomach. 134 (6) (2012) 061033-1–061033–10.
[32] S.M. Reddy, J.M. Mallikarjuna, V. Ganesan, flow and heat transfer analysis through a brake disc—A CFD approach, in: Proceedings of the ASME 2006 International Mechanical Engineering Congress and Exposition, vol. 3, ASME, Chicago, Illinois, USA, 2006, pp. 481–485.
[33] P.D. Richardson, O.A. Saunders, Studies of flow and heat transfer associated with a rotating disc, J. Mech. Eng. Sci. 5 (4) (1963) 336–342.
[34] T. Schuetz, Cooling analysis of a passenger car disk brake, SAE Technical Paper No. 2009-01-3049.
[35] D.A. Johnson, B.A. Sperandei, R. Gilbert, Analysis of the flow through a vented automotive brake rotor, ASME J. Fluids Eng. 125 (6) (2003) 979–986.
[36] H.B. Yan, T. Mew, M.-G. Lee, K.-J. Kang, T.J. Lu, F.W. kienhöfer, T. Kim, Thermofluidic characteristics of a porous ventilated brake disk, ASME J. Heat Transf. 137 (2) (2015) 022601-1–022601-11.
[37] R.M. Kelso, T.T. Lim, A.E. Perry, An experimental study of round jets in cross-flow, J. Fluid Mech. 306 (1996) 111–144.
[38] A. Belhocine, M. Bouchetara, Thermal analysis of a solid brake disc, Appl. Therm. Eng. 32 (2012) 59–67.